Electronic Supplementary Material (ESI) for Energy & Environmental Science.

Supplementary Information for

Direct observation of active catalyst surface phases and the effect of dynamic self-optimization in NiFe-layered double hydroxides for alkaline water splitting

Zhen Qiu[1], Cheuk-Wai Tai[2], Gunnar A. Niklasson[1], Tomas Edvinsson[1]*

[1]Department of Engineering Sciences, Solid State Physics, Uppsala University, Box 534, SE-75121 Uppsala, Sweden

[2]Department of Materials and Environmental Chemistry, Stockholm University, SE-10691, Stockholm, Sweden

Correspondence to: tomas.edvinsson@angstrom.uu.se.

Methods

Chemicals

Iron(III) nitrate nonahydrate $Fe(NO_3)_3 \cdot 9H_2O$ (≥98%), Nickel (II) nitrate hexahydrate ($Ni(NO_3)_2 \cdot 6H_2O$) (≥97%), urea $CO(NH_2)_2$ (≥99.5%) and ethanol (≥99.5%) were purchased from Sigma-Aldrich. Potassium hydroxide pellets were purchased from VWR. All the chemicals used here were without further purification.

Fabrication of nickel-iron based catalysts

Ultrathin nickel-iron layered double hydroxides (NiFe LDH) nanosheets in situ growing on nickel foam were prepared by the facile one-pot hydrothermal method. In a typical procedure, nickel foam (about 2.5 cm x 3 cm) was cleaned by 3 M HCl in an ultrasonic cleaner for 35 min to remove the surface oxide layer. Then nickel foam was washed by deionized water and ethanol for 6 min by ultrasound irradiation, respectively, and blown dry under a stream of compressed nitrogen. Meanwhile, 0.29 g ($Ni(NO_3)_2 \cdot 6H_2O$), 0.4 g $Fe(NO_3)_3 \cdot 9H_2O$ and 0.6 g $CO(NH_2)_2$ were dissolved in 80 ml deionized water under magnetic stirring for 30 min to ensure homogeneity. After dissolution, the aqueous solution was transferred into a 100 ml Teflon-lined stainless steel autoclave. The as-prepared nickel foam was vertically immersed into the solution with the topside protected by a Kapton tape. The in situ growth was carried out for 12 h in an oven at 120 ^{o}C. After the autoclave cooling down to room temperature naturally, the resultant sample was ultrasonically washed by deionized water and ethanol in sequence for 6 min to remove the residual reactants and then dried at 80 ^{o}C for 12 h in air. The aged catalysts were gained after 100 h operation at 1.7 V in 1M KOH using the two-electrode configuration. The obtained anodic and cathodic catalysts were denoted O-NiFe LDH and H-NiFe LDH, respectively. In comparison, $Ni(OH)_2$ was synthesized using the same procedure without 0.4 g $Fe(NO_3)_3 \cdot 9H_2O$.

Characterization techniques

Electron microscopy and spectroscopy

The surface morphologies and elemental distribution before and after operation were observed by a scanning electron microscopy (SEM, Zeiss 1550, In-lens detector, 5-10 kV) with an energy-dispersive X-ray spectroscopy (EDS) detector. The transmission electron microscopy (TEM) study was carried out with a JEOL JEM-2100F microscope operated at 200 kV and equipped with a Gatan Ultrascan 1000 CCD camera, Gatan STEM BF/DF detectors, and a post-column energy filter (GIF Tridiem). High-angle annular dark-field scanning transmission electron microscopy (HAADF-STEM), also known as Z-contrast imaging, and electron energy loss spectroscopy (EELS) analyses were also conducted using the same microscope. The probe size and camera length used were 0.5 nm and 2 cm, respectively. The probe size and scanning rate were optimized to have a reasonably good signal-to-noise ratio and to minimize beam damage. EELS spectra for the oxygen K edge (c.a. 532 eV), Fe L edge (c.a. 708 eV) and Ni L edge (c.a. 852 eV) were acquired in STEM mode. The precision of the energy is about +/-0.2 eV. Data acquisition and processing were done in Gatan Microscopy Suite. All EELS spectra were acquired at the regions of which the inelastic mean free paths are between 0.3 and 0.8. The contribution of multiple scattering in EELS spectra was removed by the Fourier-ratio deconvolution of low loss features. Power-law background model was also applied. In the study of Fe and Ni oxidation states, the estimation was done by measuring the integrated L_3/L_2 intensity ratios using double arctan continuum model, which has been applied to many EELS spectra for analysis of 3d transition metals and their compounds[1, 2]. The detailed procedures can be found in previous works[3]. The samples were scratched off from the substrate with a diamond scriber onto a TEM grid with holey carbon supporting films.

X-ray diffraction (XRD)

X-ray diffraction (XRD) measurements were carried out with a Siemens D5000 Diffractometer in the parallel beam geometry with an X-ray mirror and a parallel plate collimator of 0.4^{o}. The data was collected under CuK_{α} X-ray source (λ = 1.54 Å) with 1^{o} incidence angle and 2θ ranging from 20^{o} to 85^{o}, using 0.05^{o} per step.

X-ray photoelectron spectroscopy (XPS)

X-ray photoelectron spectroscopy (XPS) was carried out on a PHI Quantum 2000 spectrometer with monochromated Al Kα radiation with a 45° angle of electron emission. In order to ensure the peak position, the highly oriented pyrolytic graphite (HOPG) as a calibration was attached to the as-prepared samples. The wide scan spectra were performed from 0 to 1100 eV (binding energy range), using 224 eV pass energy and 0.8 eV per step. The high-resolution XPS spectra for Ni 2p, Fe 2p, O 1s, and C 1s were recorded with a pass energy of 26 eV and a step energy of 0.05 eV. The electron and ion neutralization were used during all measurements. The resulting spectra were analyzed by CasaXPS software. All the peaks were calibrated with the C 1s spectrum binding energy of 284 eV of HOPG.

Ex-situ Raman spectroscopy

Raman spectroscopy was measured in air on a confocal Raman microscope (RM 1000, Renishaw) using a 532 nm doubled Nd: YAG laser with 5 mW laser power and an 1800 lines/mm grating. All Raman spectra were collected with a resolution is ~1 cm^{-1}. Acquisition time for each spectrum was 10 s from 100 to 2000 cm^{-1}. All spectral peaks were calibrated against the value of 520.7 cm^{-1} of a silicon wafer.

In situ Raman spectro-electrochemistry

All in situ Raman measurements were performed with a custom-made spectro-electrochemical cell as shown in Fig. S13. The electrochemical activities were measured in a three-electrode configuration at room temperature. The as-obtained catalyst, a Pt wire and Ag/AgCl (3M) were used as a working electrode, counter electrode, and reference electrode, respectively. In situ Raman spectra of the working electrode were recorded for 30 min during a current-time (i-t) curve at selected potentials using a confocal Raman microscope coupled with a 90-degree angled Olympus 10x objective. The electrochemical cell was made of quartz and stood in front of the objective. The 532 nm laser with a power of 50 mW at the objective was used to generate Raman spectra. Acquisition time for each spectrum was 10 s with 10 sweeps from 100 to 2500 cm^{-1}. Other operations were the same as above. All spectra were normalized based on the Raman peak at ~140 cm^{-1}. In order to identify detectable interfacial species during different gas evolution, Raman spectra were collected with different bias on a nickel hydroxide electrode under the same condition. To gain insight into the function of Fe during water electrolysis, NiFe LDH and $Ni(OH)_2$ spectra were taken under the same conditions.

Photoluminescence (PL) spectroscopy

Photoluminescence spectra were performed by a 325 nm laser on as-prepared TEM samples at room temperature. The acquisition time was 10 s in the range of 1.7-3.8 eV. The spectral shift was calibrated against the 1332 cm^{-1} line of diamond.

Fourier transform infrared (FT-IR) spectrometry

FT-IR spectra were measured by accumulating 256 scans at 4 cm^{-1} resolution in the range of 600–4000 cm^{-1} using a vacuum-pumped FTIR spectrometer (Bruker IFS66v/s). The spectrometer is equipped with an external HgCdTe liquid nitrogen cooled detector, which is connected with an UHV chamber via KBr windows thus keeping the entire beam path under vacuum.

Electrochemical measurements

All electrochemical measurements were carried out in 1 M KOH (degassed with N_2 for 2h before the reaction) on a CHI760C electrochemical workstation or Zahner workstation at room temperature. All current densities were normalized to the geometrical area. In a three-electrode configuration, as-prepared catalysts, a Pt mesh (2 cm × 1 cm), and Ag/AgCl (3M KCl) were used as the working electrode, the counter electrode, and reference electrode, respectively. The working electrode and the counter electrode were separated by a glass frit. Cyclic voltammetry (CV) plots at a scan rate of 200 mV s^{-1} were performed for 20 cycles prior to recording linear scan voltammetry (LSV) at 5 mV s^{-1} for the fresh sample. Unless where stated, all data were directly used without any iR compensation. The measured potential was converted into the RHE scale according to the following equation: $E_{RHE} = E_{measured} + 0.21 + 0.059 \times pH$ (pH = 14 ± 0.2). The overpotential (η) for anode and cathode can be described as follows:

$$4e^- + 4H_2O \Leftrightarrow 4OH^- + 2H_2 \qquad \eta_{cathode} = E_{RHE} - 0\ V$$

$$4OH^- \Leftrightarrow 2H_2O + 4e^- + O_2 \qquad \eta_{anode} = E_{RHE} - 1.23\ V$$

Electrochemical impedance spectroscopy (EIS) tests were performed at different overpotentials versus RHE in the frequency range of 1-100 kHz using an a.c. signal of 10 mV amplitude. The Tafel slope was recorded at a scan rate of 5 mV s^{-1} and calculated by the following equation, $\eta = b \times logJ + a$, where J was obtained with 100% iR correction, R is the internal resistance of the electrochemical cell obtained from EIS, η is the overpotential and b is the Tafel slope. The electrochemical active surface area (ECSA) is a vital factor to determine the electrochemical activity. To study the ECSA of as-prepared catalysts, we used CV measurements by different scan rates in the non-faradaic potential range vs RHE. Since the ECSA is directly proportional to the double-layer capacitance (C_{dl}), the obtained C_{dl} can be used to represent the ECSA. The C_{dl} can be obtained by the equation $C_{dl} = \frac{dQ}{dU} = \frac{dQ/dt}{dU/dt} = \frac{dJ}{dv}$, where Q is the charge associated with movement of electrolyte ions and adsorption/desorption at the electrode-electrolyte interface, U is the applied potential, J is the corresponding current density and v is the scan rate. The multi-current process was performed with the same experimental setup. The overall water splitting reaction was characterized using a two-electrode configuration in 1 M KOH at a scan rate of 5 mV s^{-1}. Experiments involving LSV, multi-chronopotentiometry and i-t curve were conducted under continuously rotation at 500 rpm to get rid of the generated bubbles. The equilibration time for all electrochemical measurements was 10 s.

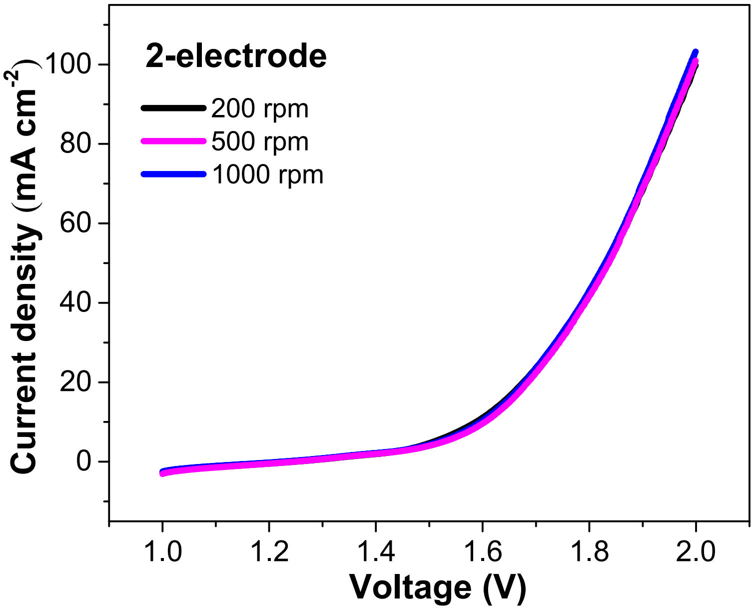

Fig. S1. Polarization curves of NiFe bi-functional catalysts as a cathode and an anode with different magnetic stirring at 200 rpm, 500 rpm, and 1000 rpm. The current density presents negligible change with different magnetic stirring, which indicates that magnetic stirring does not influence the reaction kinetics.

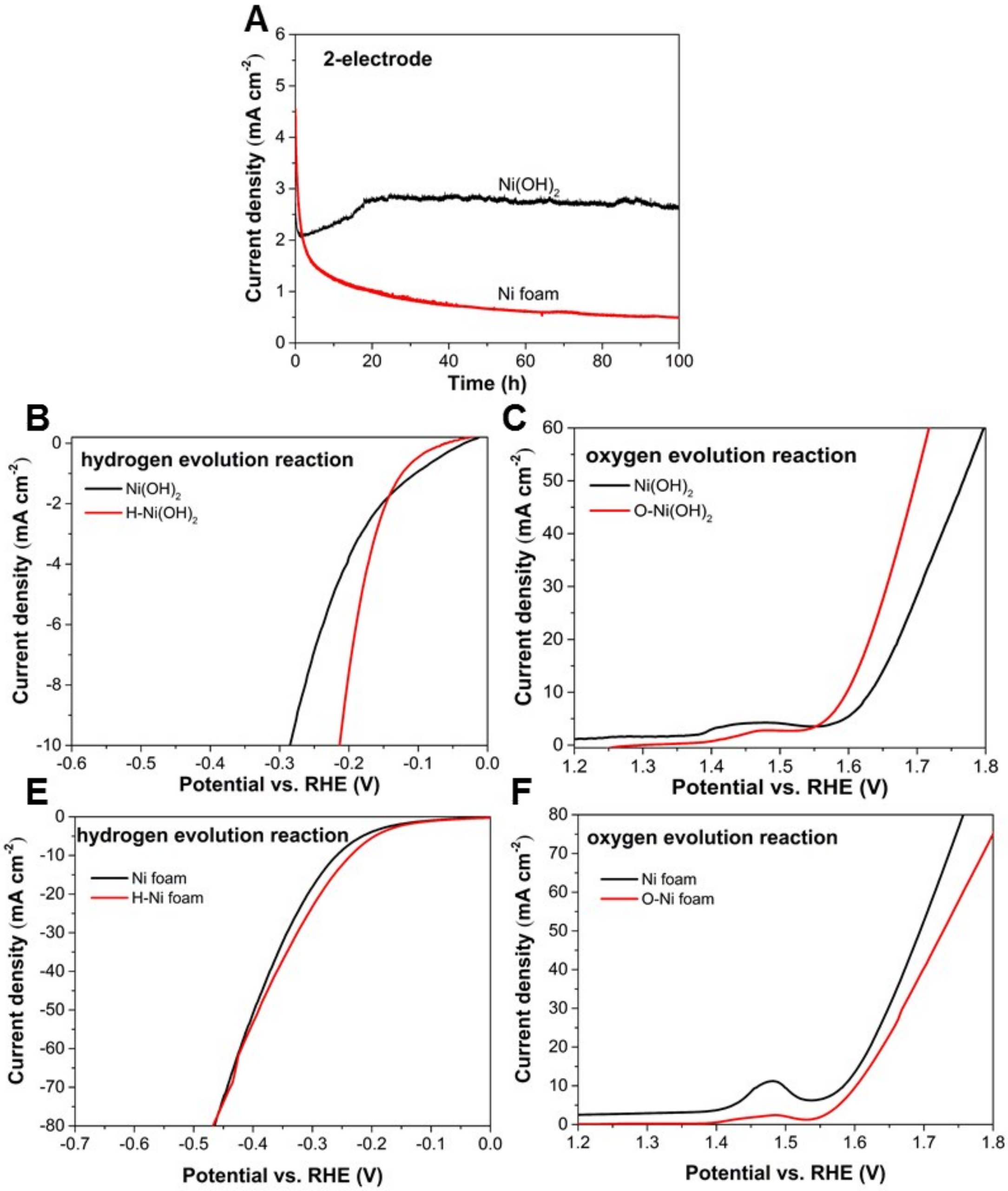

Fig. S2 (A) J-t curve obtained with Ni foam and Ni(OH)$_2$ in a two-electrode configuration at 1.7 V applied voltage in 1 M KOH without iR-correction. (B, E) HER and (C, F) OER polarization curves of pristine and aged Ni foam and Ni(OH)$_2$ in a three-electrode configuration versus the RHE potential scale. All scan rates were 5 mV s^{-1}.

Table S1. Comparison of the electrocatalytic HER and OER performance of as-obtained catalysts at 10 mA cm^{-2} in 1 M KOH

Working electrode	**η_{HER} (mV) @10 mA cm^{-2}**	**Working electrode**	**η_{OER} (mV) @10 mA cm^{-2}**
NiFe LDH	-204	NiFe LDH	182
H-NiFe LDH	**-59**	**O-NiFe LDH**	**184**
Ni foam	-259	Ni foam	355
H-Ni foam	-235	O-Ni foam	373
$Ni(OH)_2$	-284	$Ni(OH)_2$	402
H-$Ni(OH)_2$	-214	O-$Ni(OH)_2$	368

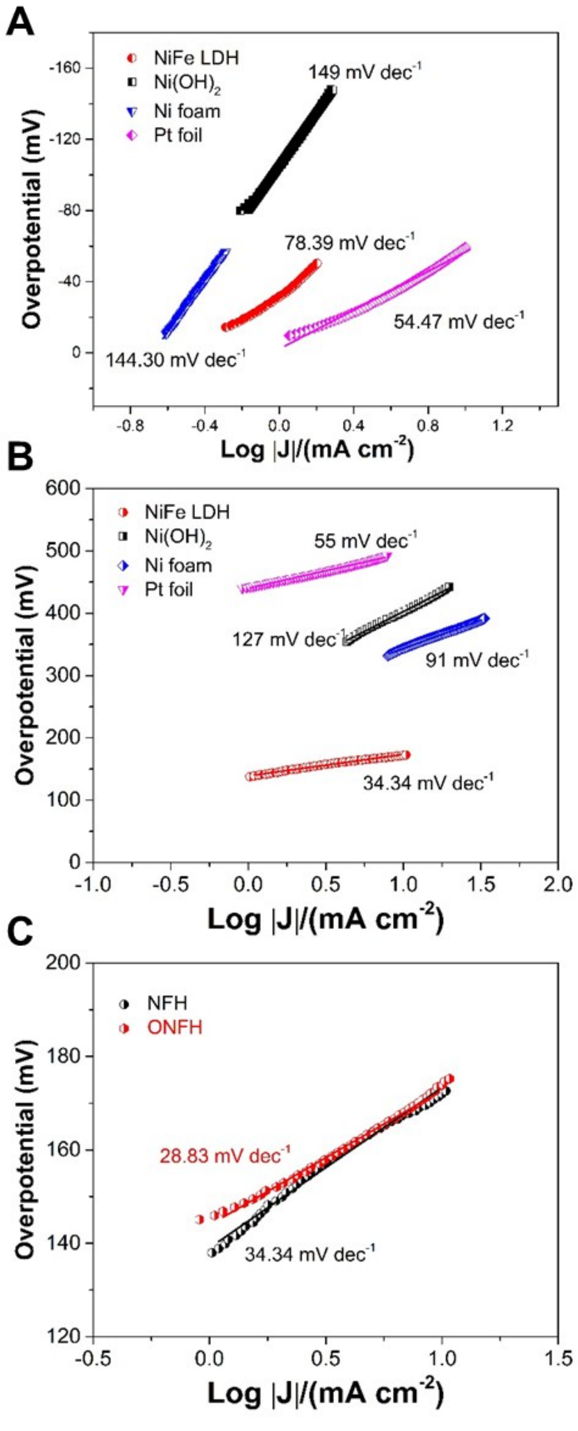

Fig. S3. The iR-corrected Tafel slope of different catalysts for (A) HER and (B) OER in 1 M KOH at a scan rate of 5 mV s^{-1}. (C) The Tafel plot comparison of NiFe LDH and O-NiFe LDH catalysts for oxygen generation under the identical situation.

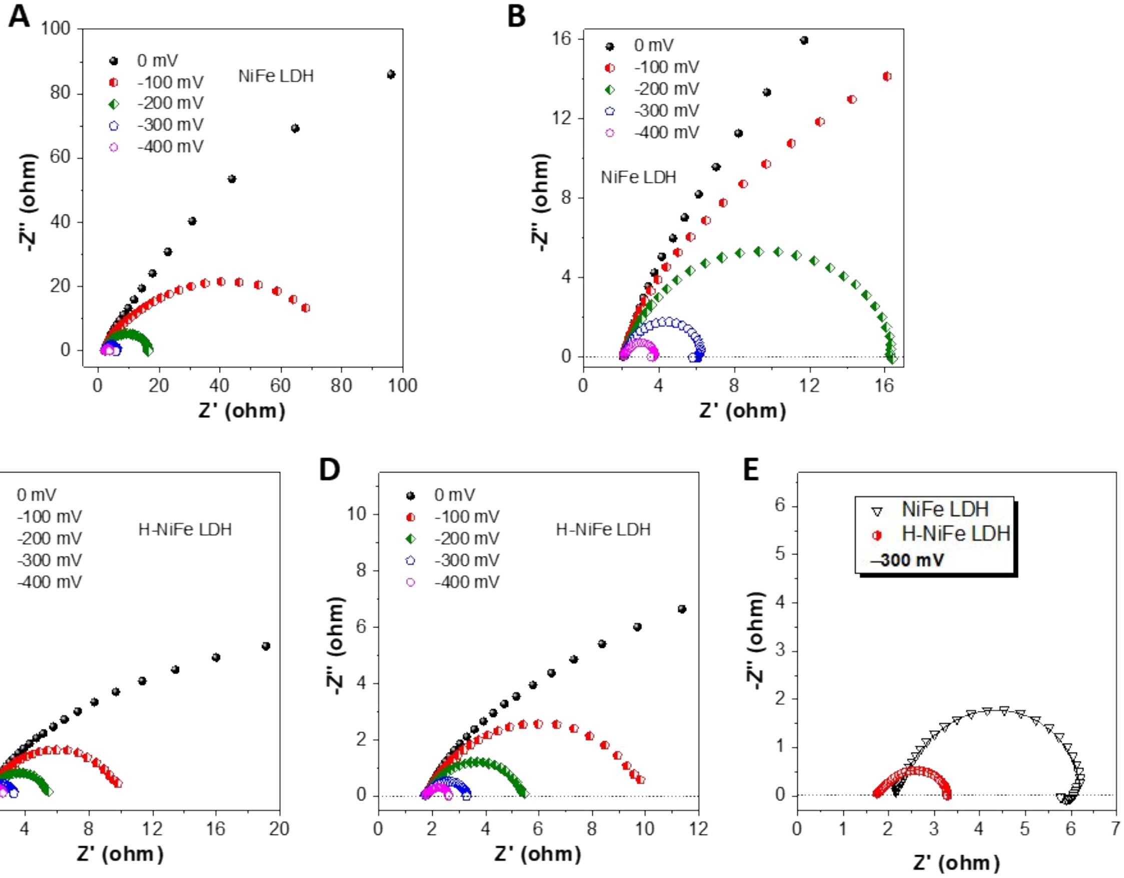

Fig. S4. Representative Nyquist plots for (A) NiFe LDH and (C) H-NiFe LDH catalysts at different overpotentials versus RHE, respectively. (B) and (D) are the corresponding magnification of (A) and (C). (E) is the comparison of impedance spectra for NiFe LDH (black triangle) and H-NiFe LDH (red diamond) measured at -300 mV overpotential. Fig. S4E clearly shows the smaller semicircle diameter and weaker inductive behavior of H-NiFe LDH than that of NiFe LDH.

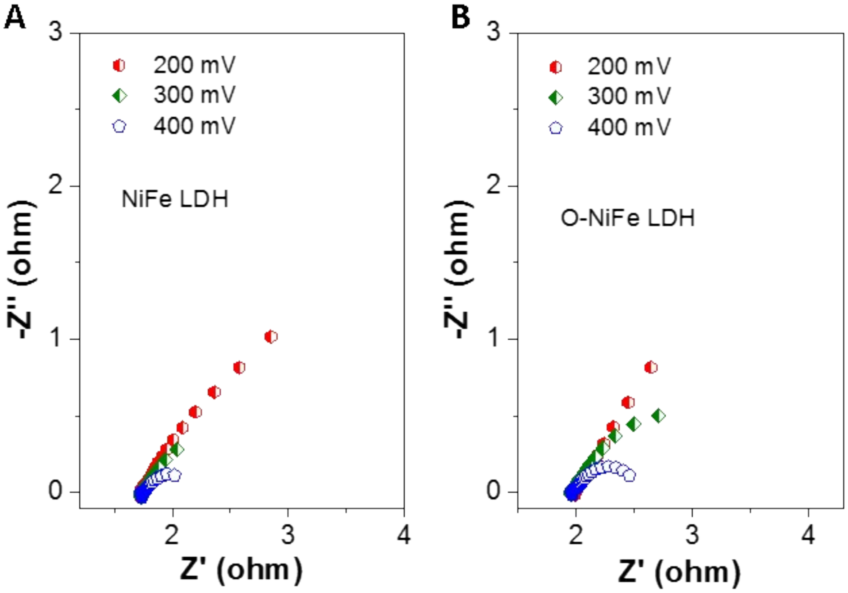

Fig. S5. Representative Nyquist plots for (A) NiFe LDH and (B) O-NiFe LDH catalysts at different overpotentials versus RHE, respectively. The impedance data exhibit semicircular arcs at 400 mV overpotential with similar reaction resistances (around 1 ohm) for NiFe LDH and O-NiFe LDH, indicating there is not much difference in their reaction barrier.

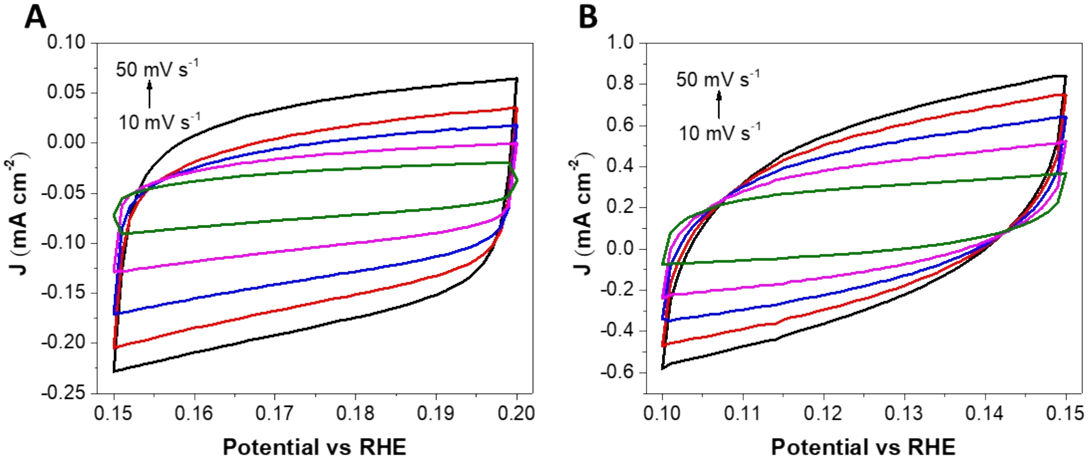

Fig. S6. CV curves of (A) NiFe LDH and (B) H-NiFe LDH catalysts with various scan rates under the non-faradic range versus RHE.

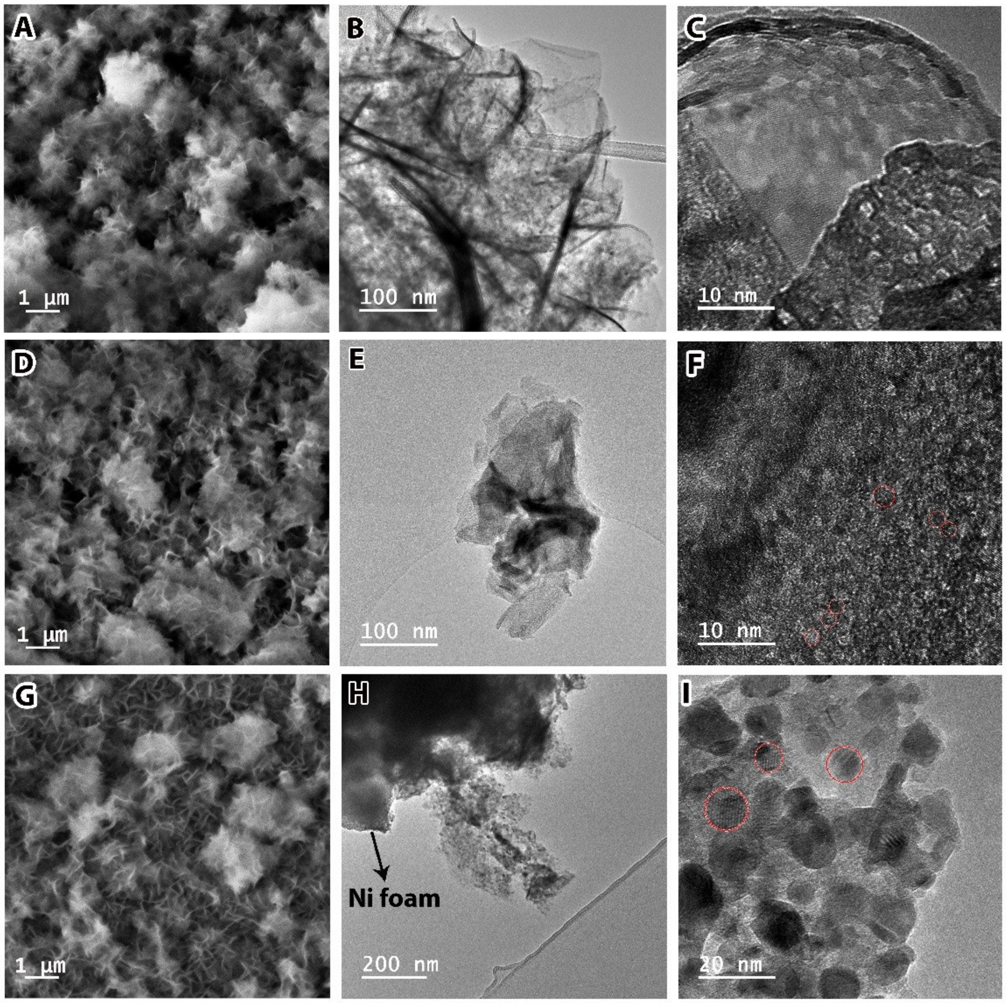

Fig. S7. SEM images of (A) initial NiFe LDH catalysts, (D) post-100 h OER testing and (G) post-100 h HER testing at the applied potential 1.7 V. TEM images of (B) NiFe LDH, (E) O-NiFe LDH and (H) H-NiFe LDH catalysts . Corresponding HRTEM images of (C) NiFe LDH catalysts, (F) post-100 h OER testing and (I) post-100 h HER testing.

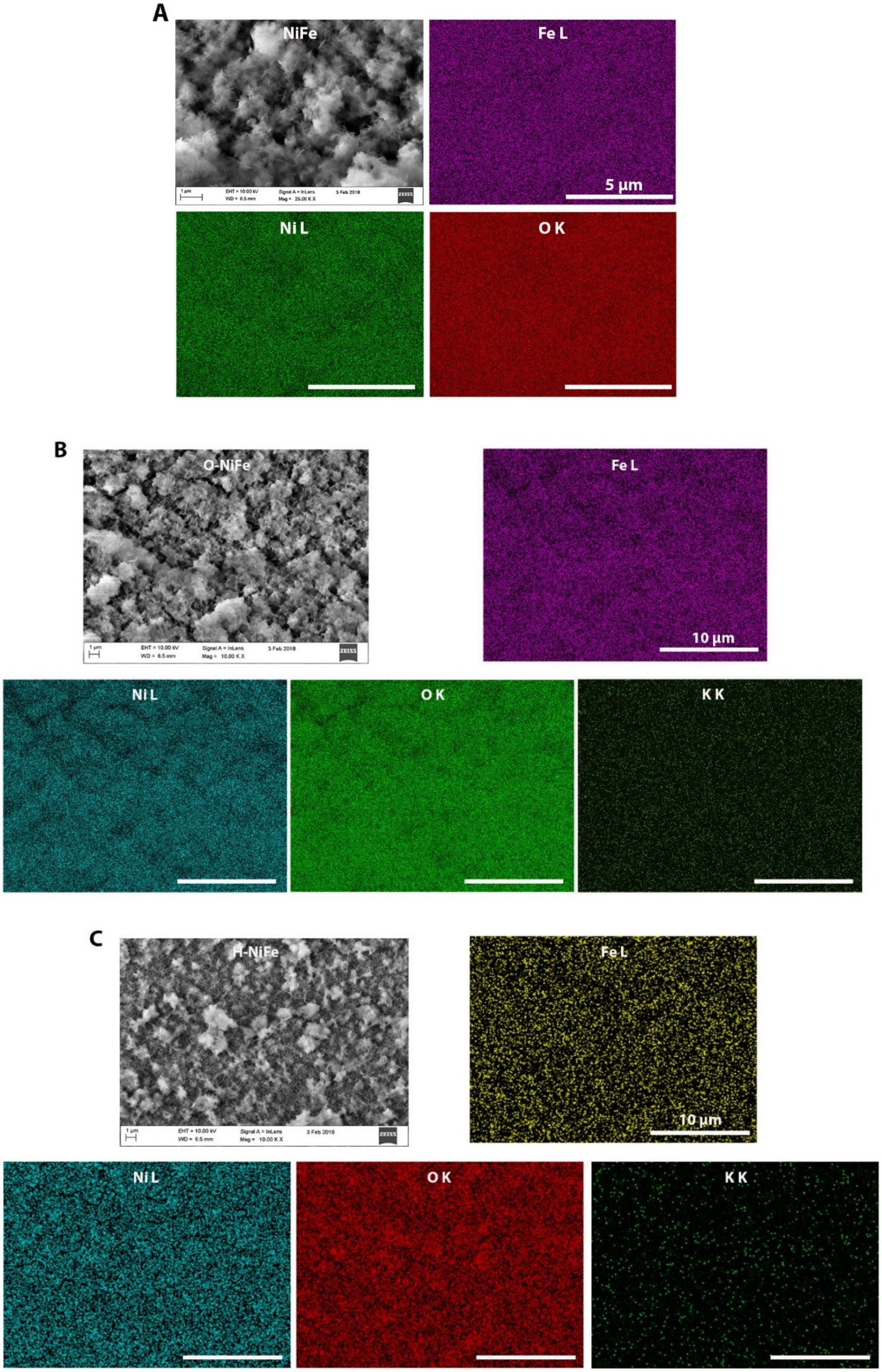

Fig. S8. EDS mapping results of (A) NiFe LDH, (B) O-NiFe LDH, and (C) H-NiFe LDH. They show the uniform distribution of Fe, Ni, and O in all of as-obtained catalysts. The element potassium in B and C is from the electrolyte 1 M KOH, which is consistent with XPS data.

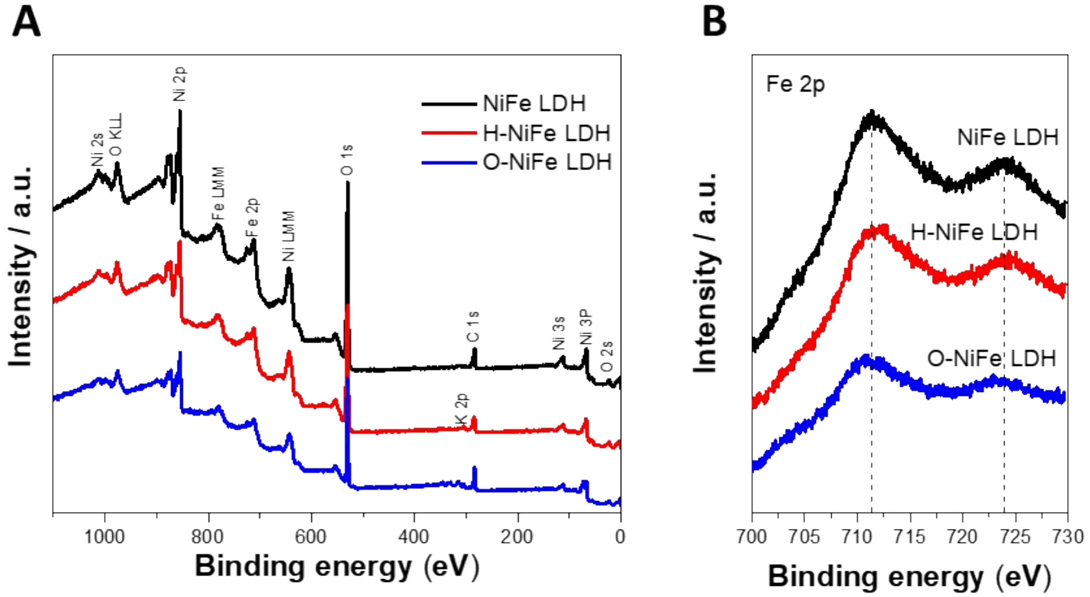

Fig. S9. (A) XPS survey spectra and (B) High-resolution XPS spectra of Fe 2p for NiFe LDH based catalysts before (NiFe LDH) and after 100 h HER (H-NiFe LDH) and OER (O-NiFe LDH) process.

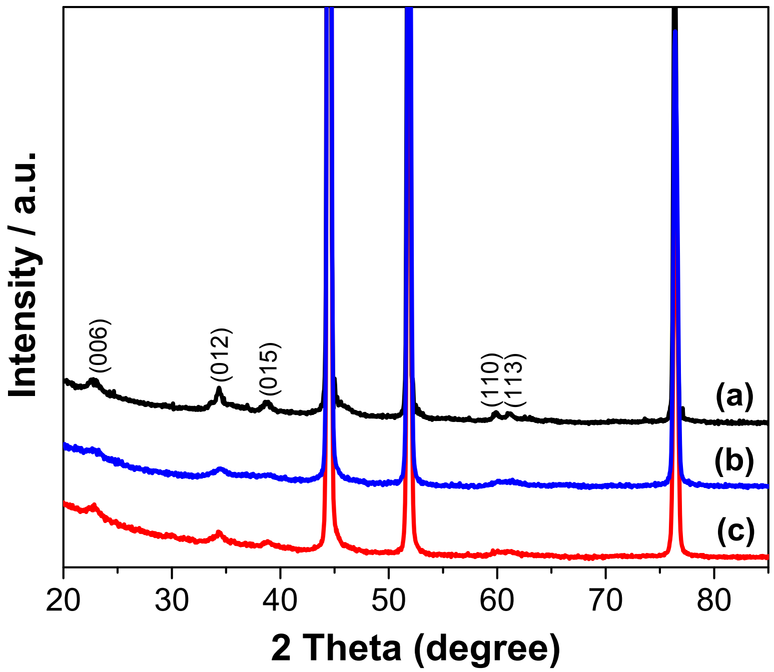

Fig. S10. XRD characteristics of the as-obtained catalysts grown on Ni foam (a) NiFe LDH (b) O-NiFe LDH (c) H-NiFe LDH. XRD characteristics of all catalysts were consistent with the standard XRD pattern of nickel-iron carbonate hydroxide hydrate (NiFe-CO_3 LDH, reference code: 00-049-0188) [4, 5].

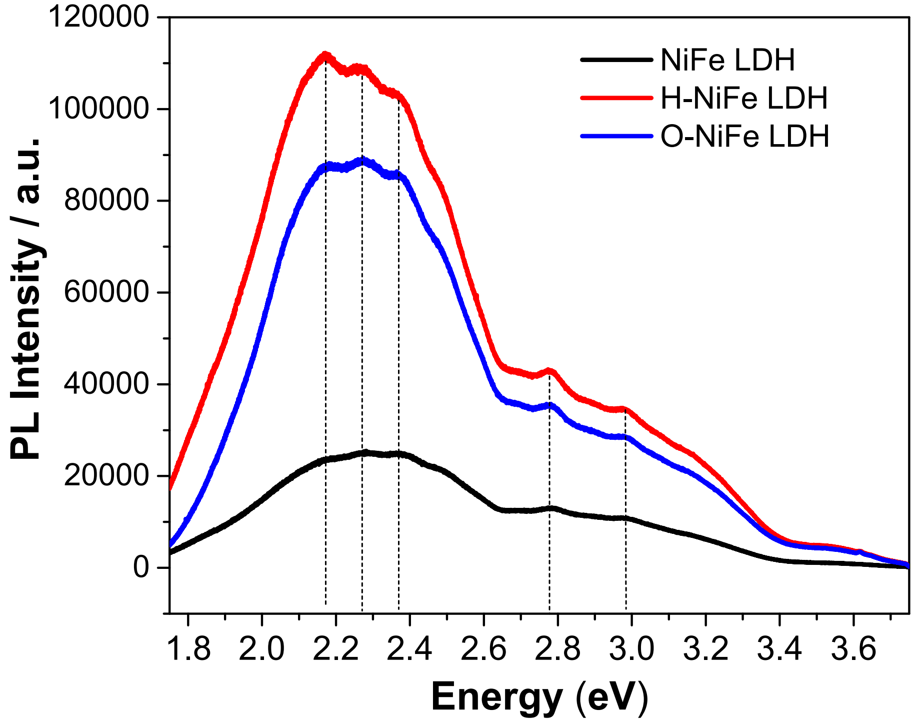

Fig. S11. Photoluminescence (PL) of the as-obtained catalysts.

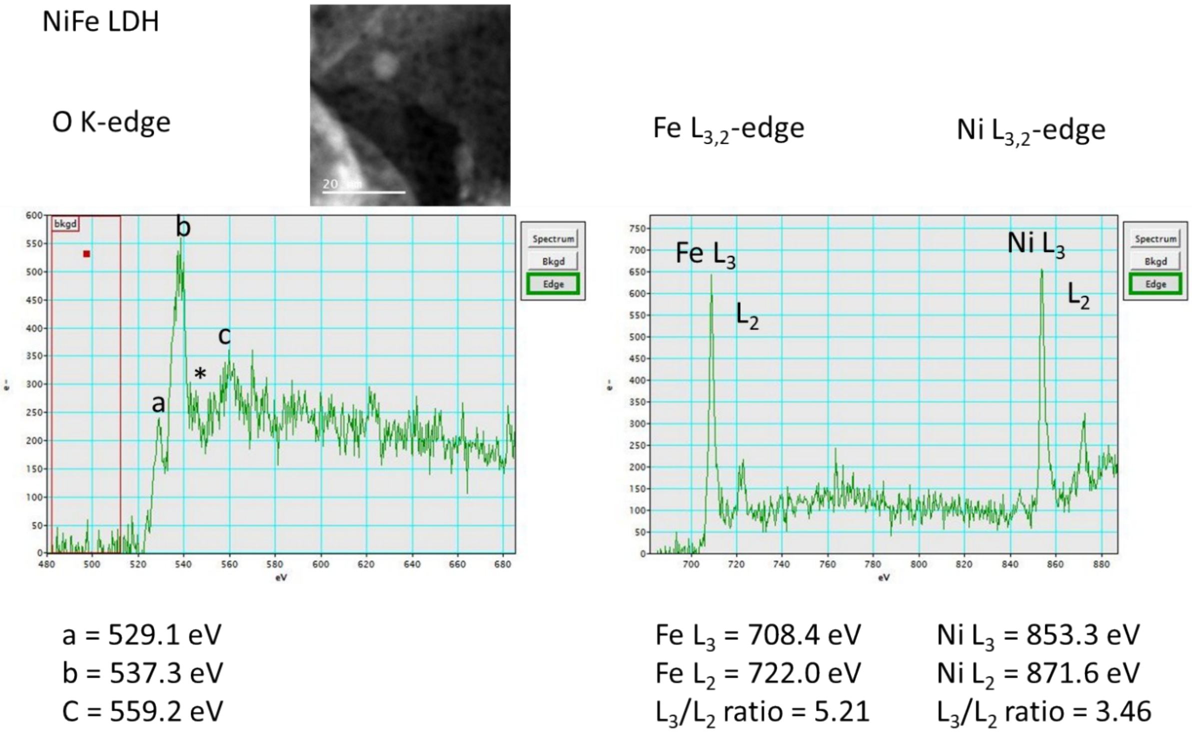

O-NiFe LDH

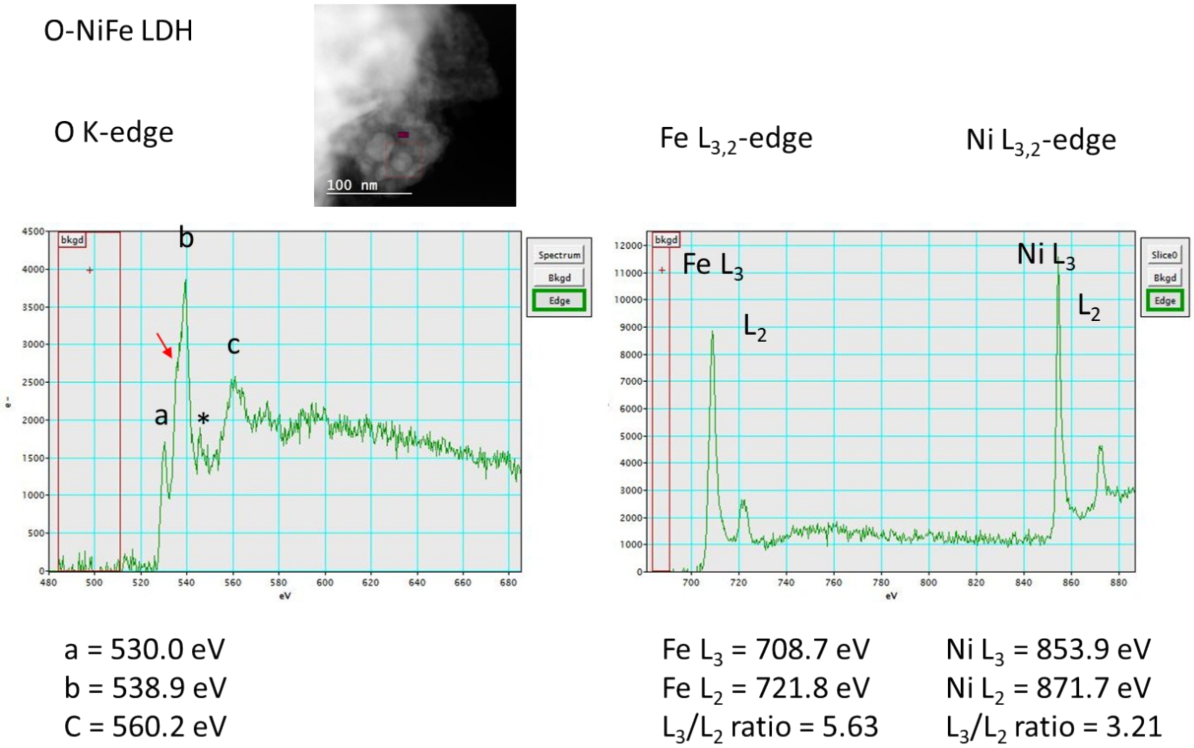

H-NiFe LDH

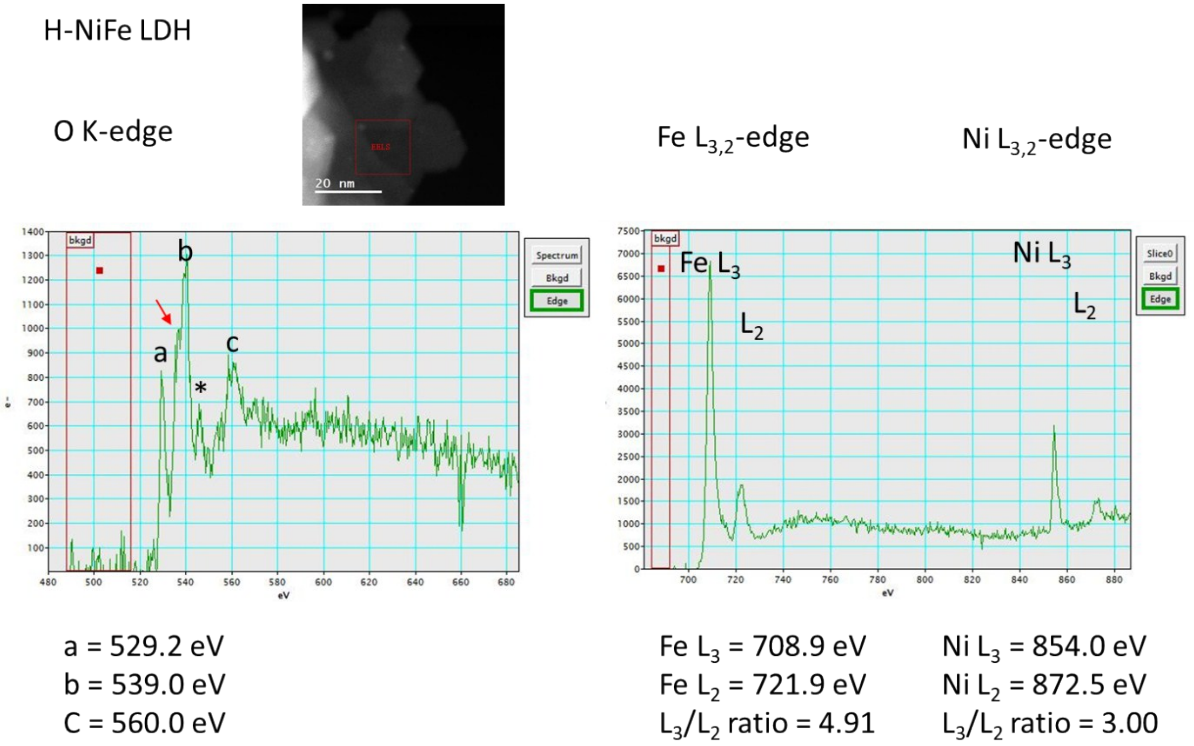

Fig. S12 EELS spectra of NiFe LDH, O-NiFe LDH and H-NiFe LDH showing K-edge of O and L$_{3,2}$ edges of Fe and Ni and intensity integration.

In Fig. S12, Fe and Ni $L_{3,2}$ edges of all three samples show their white-line features, of which the high intensity is due to the high density of unoccupied 3d states. The L_3 and L_2 correspond to excitations from the spin-orbit slit levels $2p_{3/2}$ and $2p_{1/2}$. In all three samples, the $L_{3,2}$ edges of Fe and Ni and K-edge of O are quite similar in term of energy range and general features (Fig. S12). In the K-edge of O, three main peaks, labeled as “a”, “b” and “c”, are found at about 530 eV, 537 eV, and 559 eV, respectively. The peaks of the $L_{3,2}$ edges of Fe and Ni are located at ~708 and 722 eV and 853 and 872 eV, respectively. The peaks did not shift significantly and varied within the error (+/-0.2eV), indicating that the material phases remained during different treatments. The total integral intensity ratio (L_3/L_2) is correlated to the oxidation state of Fe and Ni. H-NiFe LDH has the lowest Ni L_3 / L_2 ratio, i.e. having the lowest valence. Since the separation between Ni L_3 and L_2 remains ~18.0eV, we deduced that the change of the ratio in different samples is due to the oxygen bond influenced by Fe. We did not consider the presence of NiO_2 and other $MNiO_2$ (where M is metal) because the corresponding L_3 and L_2 edges are higher than 856 and 873 eV, respectively, and considerable broadened L_3 edges were not observed [6, 7]. The $L_{3,2}$ edges of Fe in all samples are similar. The variation of the peak positions is within the experimental errors. The energy difference between L_3 and L_2 is 13 eV. It is known that this separation is rather stable regardless of phases [8], although the exact energy position is sensitive to the bonding conditions or phases, especially in oxides and hydroxides. However, the Fe L_3 / L_2 ratio changes considerably, ranging from 4.91 to 5.63, indicating valence composition changes slightly in different samples. Unfortunately, the white-line ratio in Fe does not have a monotonic relation with its valence states. In fact, it is very sensitive to coordination geometry and local environments, besides oxidation states. However, the doublet at L_3 edge, which is given by the co-existence of Fe^{2+} and Fe^{3+}, is not observed. It can be deduced that the two distinct valences at different local chemistry environments are not the case in all three samples. Therefore, the O K-edges, which is easier to reflect the electronic structure, should be investigated. We can see that the features of O K-edges in all three samples are very similar to the one from Fe_3O_4 [8]. The three main peaks labeled as "a", "b", "c" and a fourth one labeled "*" can be observed. The strong "a" peak below 530 eV is a sign indicating that the dominant state is not pure 2+. The peaks "b" and "c" are common features in many iron-oxygen compounds. In addition to the presence of peak "*", the location of pre-edge peak "a" and the profile of peak "c" are the evidence of Fe_3O_4-like phase. Besides, there is a rather small feature close to "b", marked by a red arrow. This locates at the energy lower than 539 eV, and can be attributed to Ni (d^8)-O bond.

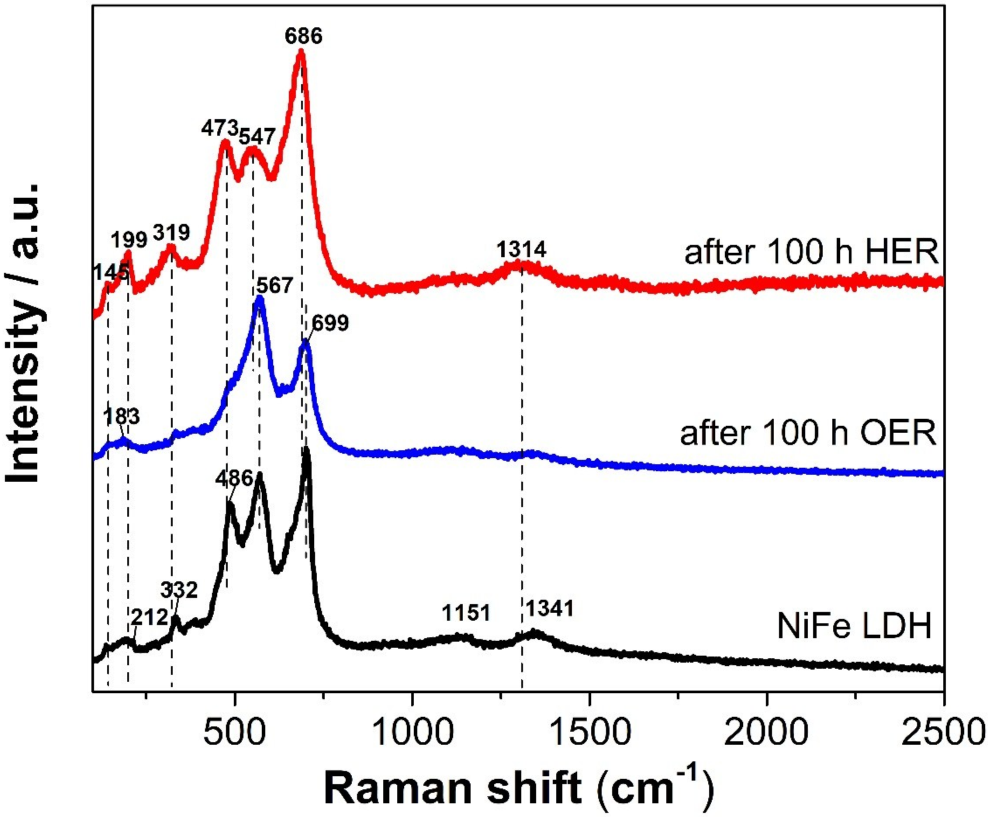

Fig. S13 Raman spectra of pristine NiFe LDH and post 100 h water electrolysis measured in the ambient air.

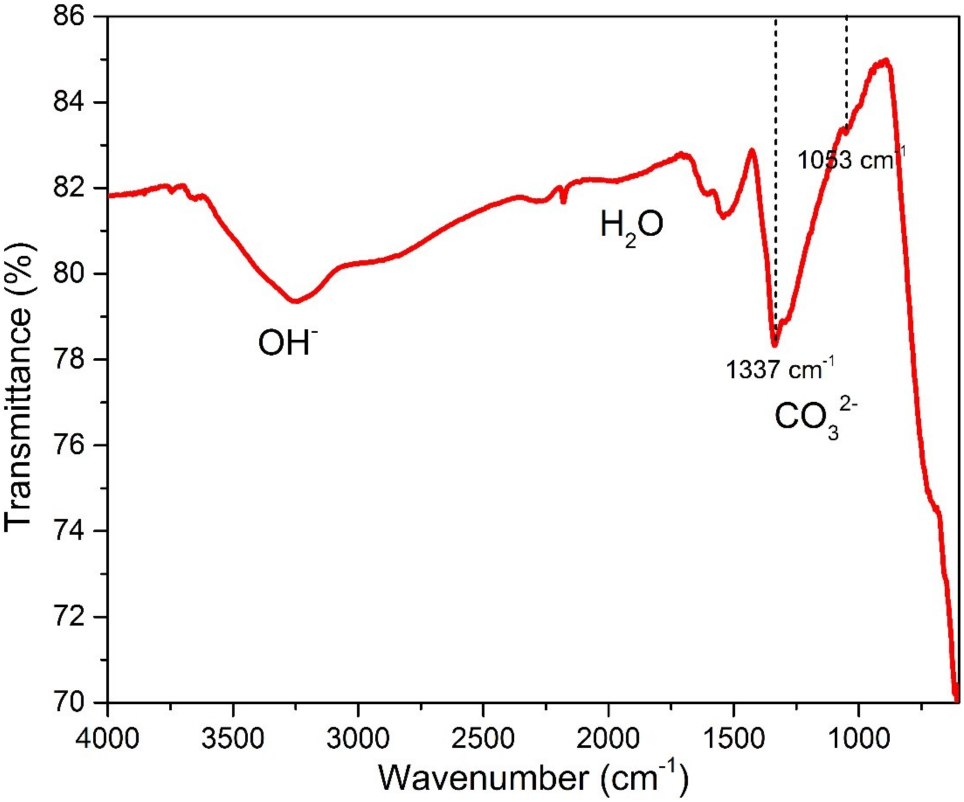

Fig. S14 FT-IR spectra of the NiFe LDH in vacuum condition.

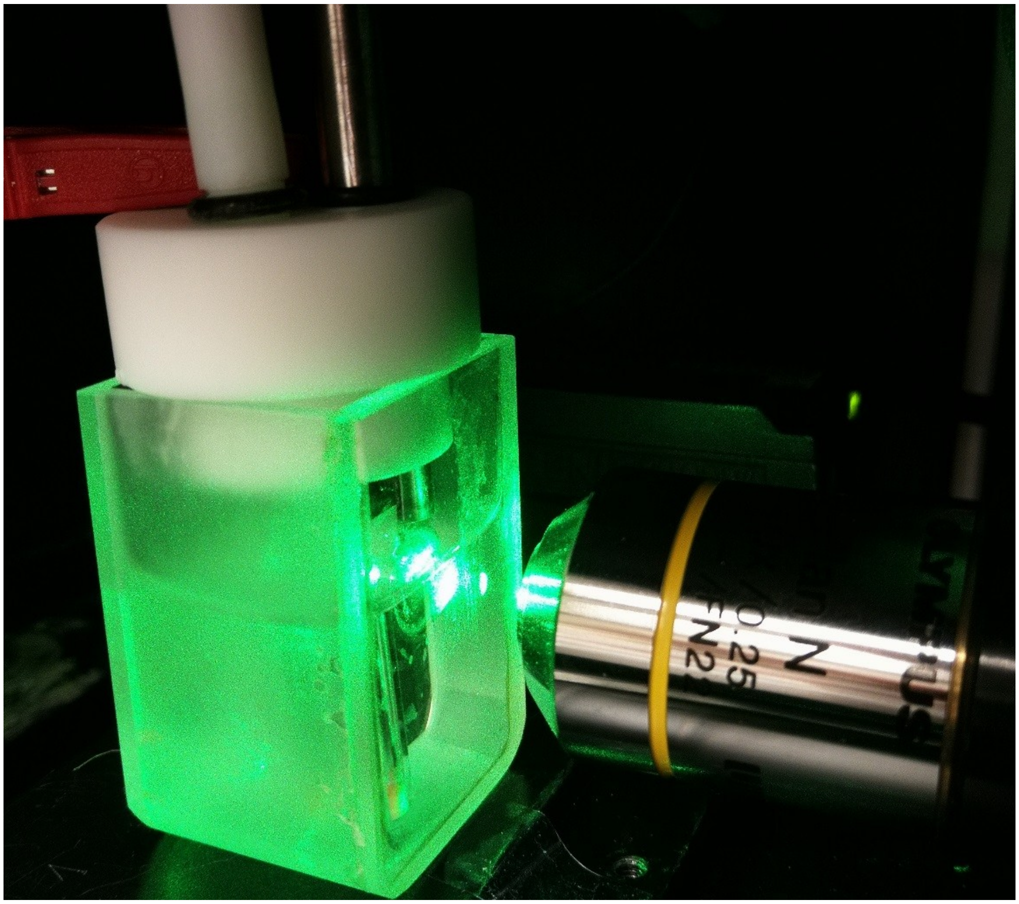

Fig. S15 Experimental setup while measuring potential dependent Raman spectra.

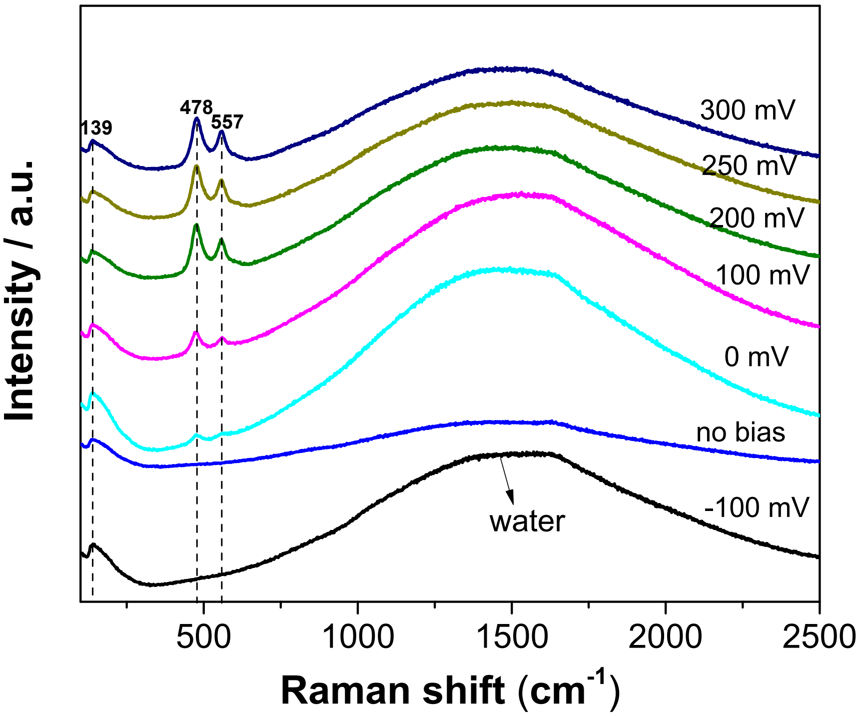

Fig. S16. In situ Raman spectra collected in 1 M KOH with different applied overpotentials versus RHE from -100 mV to 300 mV for $Ni(OH)_2$ on Ni foam. The peaks appear at~478±1 and~557±1 cm^{-1}, indicating the transformation of $Ni(OH)_2$ to NiOOH during oxygen evolution reaction in alkaline media.

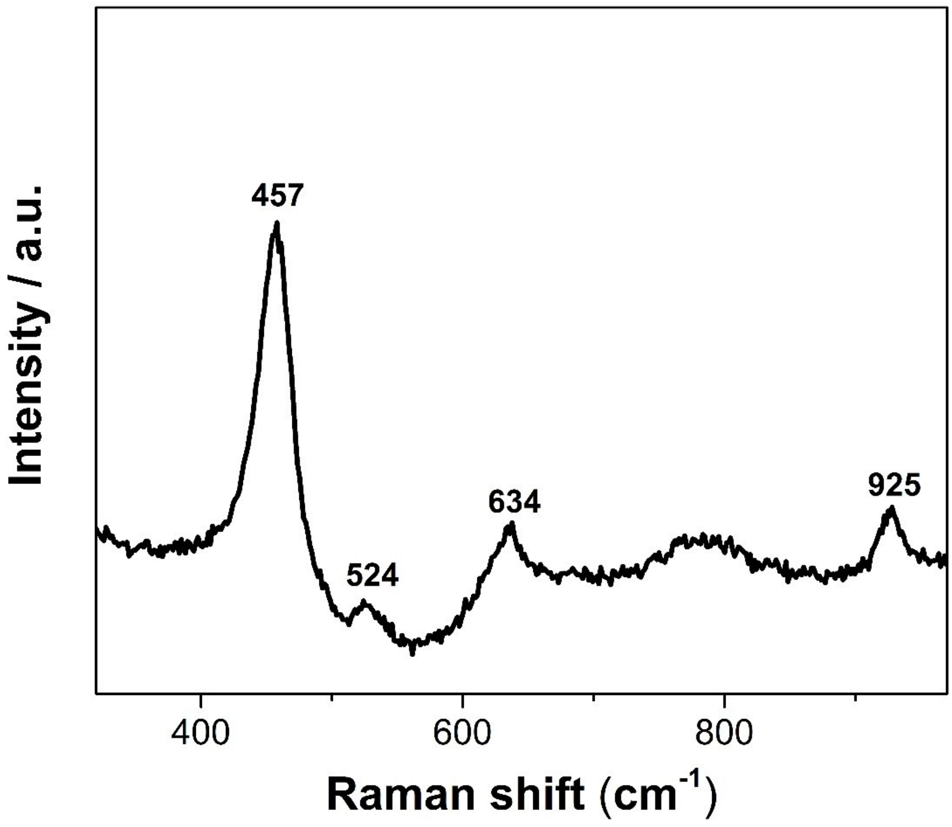

Fig. S17. Polarized Raman spectra of Ni(OH)$_2$ catalysts at room temperature.

As we know, the peak intensity is proportional to the Raman cross-section, which is due to resonance effects. The Raman bands at 457 and 524 cm^{-1} are well assigned to Ni(OH)$_2$ [9]. However, the high Raman cross section of the Ni(OH)$_2$ vibrations limits the amount of information we can extract from the Fe phases with low resonance information in catalysts. Then we used 532 nm excitation source to collect as much information of species transformation as we can during the gas evolution reaction.

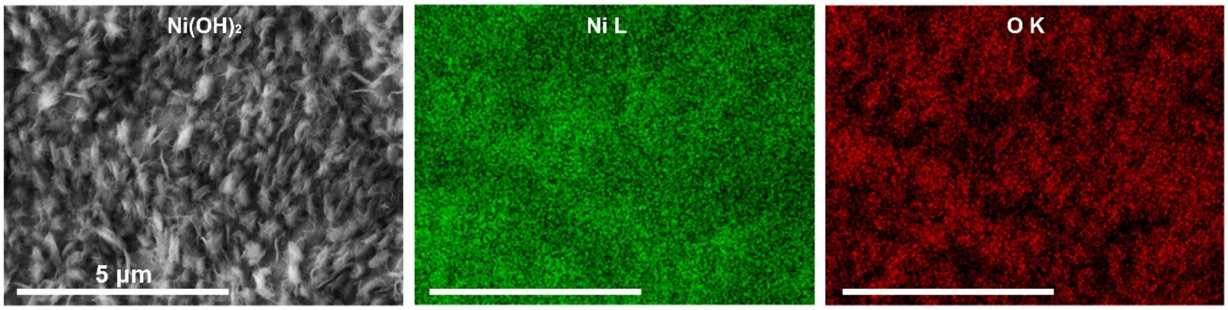

Fig. S18. SEM and the corresponding EDS mapping of $Ni(OH)_2$ on Ni foam. They show the uniform distribution of Ni and O in the as-prepared catalyst.

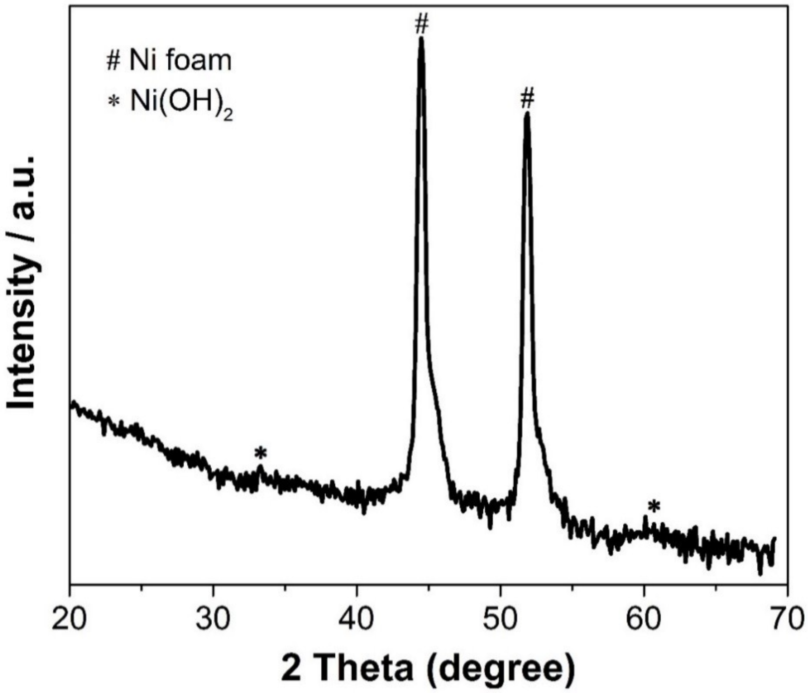

Fig. S19. XRD pattern of $Ni(OH)_2$ on Ni foam. Here, two major diffraction peaks and two small diffraction peaks are observed. The reflections of two major peaks is indexed to Ni, while, the reflections of two small diffraction peaks can be indexed to $Ni(OH)_2$ (ICSD: 00-014-0117).

Table S2. Comparison of *in-situ* Raman shifts on NiFe LDH and $Ni(OH)_2$ in 1 M KOH.

η_{HER} (mV)	Raman shift (cm^{-1})		η_{OER} (mV)	Raman shift (cm^{-1})	
	NiFe LDH	$Ni(OH)_2$		NiFe LDH	$Ni(OH)_2$
No bias	455, 526	/	No bias	455, 526	/
0	455, 526	/	0	455, 526	478, 557
-100	455, 526	/	100	455, 526	478, 557
-150	455, 526, ~841	/	200	477, 540	478, 557
-200	455, 526, ~841	/	250	477, 540	478, 557
-300	455, 526, ~841	/	300	477, 557	478, 557

According to previous reports[10, 11] and our results analysis, the OER and HER on NiFe LDH undergo as following. M represents Fe active sites at low overpotentials (η < 200 mV), while, at modest overpotentials, it represents Ni active sites (η ~ 200-300 mV).

OER process:

$$MO + OH^{-} \rightarrow OH_{ads} - MO + e^{-}$$

$$OH_{ads} - MO + OH^{-} \rightarrow O - MO + H_2O + e^{-}$$

$$2O - MO \rightarrow 2MO + O_2$$

HER process:

$$H_2O + NiO + e^{-} \leftrightarrow H_{ads} - NiO + OH^{-}$$

$$H_2O + H_{ads} - NiO + e^{-} \leftrightarrow NiO + H_2 + OH^{-}$$

Supplementary References

1. N. J. A. M. Bnvoso, 1994, **79**, 411-425.
2. H. Tan, J. Verbeeck, A. Abakumov and G. J. U. Van Tendeloo, 2012, **116**, 24-33.
3. A. Mayence, M. Wéry, D. T. Tran, E. Wetterskog, P. Svedlindh, C.-W. Tai and L. J. N. Bergström, 2016, **8**, 14171-14177.
4. M. Gong, Y. Li, H. Wang, Y. Liang, J. Z. Wu, J. Zhou, J. Wang, T. Regier, F. Wei and H. Dai, *Journal of the American Chemical Society*, 2013, **135**, 8452-8455.
5. E. Uzunova, D. Klissurski and S. Kassabov, *Journal of Materials Chemistry*, 1994, **4**, 153-159.
6. Y. Koyama, T. Mizoguchi, H. Ikeno and I. Tanaka, *The Journal of Physical Chemistry B*, 2005, **109**, 10749-10755.
7. D. S. Sun, Y. H. Li, Z. Y. Wang, X. P. Cheng, S. Jaffer and Y. F. Zhang, *Journal of Materials Chemistry A*, 2016, **4**, 5198-5204.
8. C. Colliex, T. Manoubi and C. Ortiz, *Physical Review B*, 1991, **44**, 11402.
9. S. L. Klaus, *Investigations of the Oxygen Electrode*, University of California, Berkeley, 2015.
10. B. Conway and B. Tilak, in *Advances in catalysis*, Elsevier, 1992, vol. 38, pp. 1-147.
11. R. Subbaraman, D. Tripkovic, K.-C. Chang, D. Strmcnik, A. P. Paulikas, P. Hirunsit, M. Chan, J. Greeley, V. Stamenkovic and N. M. J. N. m. Markovic, 2012, **11**, 550.